Lab on a Chip

Non-contact ultrasound oocyte denudation

SCHOLARONE™
Manuscripts

1 Non-contact ultrasound oocyte denudation

2 Amir Mokhtare[1], Benyamin Davaji[2], Philip Xie[3], Mohammad Yaghoobi[1], Zev Rosenwaks[3], Amit Lal[2],

3 Gianpiero Palermo[3], Alireza Abbaspourrad[1*].

4

5 Affiliations:

6   1. Department of Food Science, Cornell University, Stocking Hall, Ithaca, NY, 14853, United

7   States

8   2. School of Electrical and Computer Engineering, Cornell University, Ithaca, NY, USA.

9   3. The Ronald O. Perelman and Claudia Cohen Center for Reproductive Medicine, Weill Cornell

10   Medicine, New York, NY, 10021, USA

11 Abstract

12 Cumulus removal (CR) is a central prerequisite step for many protocols involved in the assisted

13 reproductive technology (ART) such as intracytoplasmic sperm injection (ICSI) and preimplantation

14 genetic testing (PGT). The most prevalent CR technique is based upon laborious manual pipetting,

15 which suffers from inter-operator variability and therefore a lack of standardization. Automating CR

16 procedures would alleviate many of these challenges, improving the odds of a successful ART or PGT

17 outcome. In this study, a chip-scale ultrasonic device consisting of four interdigitated transducers

18 (IDT) on a lithium niobate substrate has been engineered to deliver megahertz (MHz) range

19 ultrasound to perform denudation. The acoustic streaming and acoustic radiation force agitate COCs

20 inside a microwell placed on top of the $LiNbO_3$ substrate to remove the cumulus cells from the

21 oocytes. This paper demonstrates the capability and safety of denudation procedure utilizing surface

22 acoustic wave (SAW), achieving automation of this delicate manual procedure and paves the steps

23 toward improved and standardized oocyte manipulation.

Introduction

Oocyte denudation is a crucial prerequisite for unequivocal evaluation of oocyte maturity and successful intracytoplasmic sperm injection.[1,2] Residual cumulus cells can potentially prevent the oocyte from being adequately manipulated and may represent a source of DNA contamination during trophectoderm biopsy for PCR-based preimplantation genetic testings.[3,4] The established manual denuding method, developed decades ago, consists of two steps; the enzymatic digestion and then the mechanical stripping of the cumulus using pipettes.[5] Hyaluronidase is commonly used to break down the hyaluronic acid of the matrix encompassing the cumulus to facilitate their dispersion.[6] Although prolonged enzymatic exposures can minimize the time and shear stress of the mechanical procedure, it has also been shown to expand the perivitelline space (PVS) and convolute the following micromanipulation.[7,8] Despite its common usage, manual pipetting for oocyte denudation little has changed over decades and still remains inefficient, labor-intensive and fatigues the embryologist. Further, it has been shown that high shear stresses during mechanical treatment can dislocate the polar body (PB) and meiotic spindle (MS) which leads to a suboptimal ICSI outcome and poor embryo development.[9,10] Finally, it has been found that the entire denudation procedure is highly skill dependent, time sensitive and frequently suffers from intra operator variability.[2,11]

Unlike semen processing, female gamete processing has rarely been scrutinized by novel microfluidic technologies.[12–14] Until recently reported processing of cumulus-oocyte-complexes (COC) were limited to the work of Zeringue et al. that suggested a microfluidic channel that pushes the cumulus to the sides of the oocyte makes them easier to pull off at a right corners.[15,16] More recently, Weng et al. developed a microfluidic chip that achieves multiple COC processing by physically shearing them against sharp corrugated walls. In their device, COC are pushed against jagged side walls in a contraction section followed by an expansion section for reorientation.[17] We also recently showed that complete and controlled denudation is achievable in a non-contact oscillatory microfluidic channel that uses a bas-relief structure to twist the flow inside the channel. In our suggested platform the

50   denudation extent is controlled by the fluid flow and frequency of oscillation.[18,19] These techniques

51   also require additional steps for preparation and delicate loading of the COCs to the devices which

52   makes the overall process prohibitively cumbersome and time consuming. In addition, constant

53   monitoring of oocytes due to the intrinsic 2D structure of chips and limited field of view (FOV) of our

54   microscope is not possible. Despite some moderate success and improvements, all methods still

55   suffer from the irreversibility of the chips. Oocytes are rare and precious cells, so any developing

56   technology should allow their recoverability at any stage in the process.[20]

57

58   Acoustofluidics, the science of micro-manipulation of fluids and microparticles using sound waves,

59   offers advantages over the skill demanding, labor-intensive requirements of manual pipetting by reducing the

60   risks of high mechanical stress exposure, cell loss, and operator variability.[21] Between the two common

61   modalities of ultrasound generation, surface acoustic waves (SAW) is preferred over bulk acoustic

62   waves (BAW) for micron scale applications in biology and medicine.[22] These applications require high-

63   frequency acoustic wave generation, lateral control of the acoustic wave and benefit from ability to use transparent

64   substrates for optical imaging systems, all of which SAW is more appropriate. [23] In addition, making standing

65   waves with SAW relaxes the limitation of using high resonant chambers and allows the use of more

66   biocompatible, transparent but acoustically dampened material like PDMS.[24,25] More importantly,

67   ultrasound waves within cell scale wavelengths and energies similar to those commonly used in

68   ultrasound imaging and diagnostic testing can be generated using planar interdigitated transducers

69   (IDTs).[26,27] This is of particular interest, since the impact of ultrasound on variety of cells in being

70   consistently examined.[28–32] Further, diagnostic ultrasound imaging has been used for more than half a

71   century in obstetrics and gynecology and their innocuity for cells has been defined and documented in

72   terms of thermal and mechanical indexes to prevent any potential cavitation and induced thermal

73   damages.[33–40]

74

75   Using ultrasound for oocyte preparation provides a substantial evolution in the process. By gently

76   shaking and squeezing the cells, it eliminates the potential damage that can be incurred using the

77 current methods for COC denudation such as zona pellucida fracture, MS dislocation, PVS

78 expansion, or oocyte activation. [2] The IDTs that produce the ultrasound waves are either embedded

79 inside or circumscribed on the periphery of the microwells similar to those commonly used by

80 embryologists for embryo development. Using grating reflectors in one direction, and a slight

81 difference in the resonance frequency in the other, we are able to switch the acoustofluidic field

82 direction by slightly altering the actuation frequency without using multiple signal ports. Such

83 capability prevents any specific pattern formation and eliminates any void regions that can prevent

84 optimal denudation. Eventually, the acoustofluidic field inside the microwell moves and tumbles the

85 cells, continuously exposing them to shear and acoustic forces to strip off the cumulus cells. We

86 demonstrate the safety and efficacy of our method by (i) measuring the acoustic field with a laser

87 doppler interferometer (ii) measuring the temperature variation by a sensitive thermal camera and (iii)

88 performing denudation and embryo development studies on mice oocytes denuded by our method

89 compared to conventional method.

Results and Discussion

90

Working Mechanism of tunable ultrasonic denudation microwell

91

92 Efficient and controlled agitation inside the microwell for effective denudation of the oocytes require

93 complete 3D mixing of the medium inside the microwell as well as twisting the fluid flow streamlines to

94 avoid any specific patterns and trapping regions. The devices' structure, design and working

95 mechanism are illustrated in Fig. 1. A PDMS microwell with different open bottom geometries (Fig.

96 S2A) is reversibly bonded to a 500-μm-thick 128° Y-cut lithium Niobate (LiNbO$_3$) substrate between

97 the center of two orthogonally symmetric IDTs (Fig. 1A). We choose microwell dimensions that were

98 similar to microwells commonly used for embryo development and time lapse measurement, that had

99 easy access for loading and unloading under a stereo microscope, and that would prevent of bubble

100 formation at the bottom of the microwell.[41] It is also important to point out the it's imperative to make

101   grooves at the bottom of the PDMS structure where it overlays the IDTs (Fig. S3.A). As shown in Fig

102   1.C-D these grooves create an air gap between the piezoelectric substrate and the microwell structure

103   that prevents SAW absorption by PDMS. PDMS is an effective sound absorber that can convert total

104   SAW energy into heat if they come into contact. [42]

105

106   To achieve thorough mixing, we established alternating 3D pressure fields inside the microwell by

107   manipulation of two orthogonal surface acoustic waves (SAW). Due to acoustic impedance mismatch

108   between air and water, the SAW propagation is disturbed upon entering the liquid filled microwell,

109   resulting in an exponential decay along the solid liquid interface (leaky Rayleigh SAW) and 3D

110   longitudinal sound wave radiation into the liquid.[43] As such, acoustic streaming in the form of laminar

111   jet flows emanate from the periphery of the microwell driven by the momentum flux transfer of the

112   beam to the fluid as the beam attenuates (propagates) through the liquid medium.[44] These 3D waves

113   launch into the liquid at a Rayleigh angle of 22° according to Snell's law $\theta = sin^{-1}(C_l/C_s)$ where C_l,

114   and C_s are sound velocity in liquid and solid substrate, respectively.[27,45] In bioengineering

115   applications, it is this efficient energy transfer characteristic that gives rise to acoustic radiation forces

116   and acoustic streaming (Eckart streaming) necessary for particle or cell manipulation inside fluid filled

117   cavities.[26,46–49] In comparison to other fluid streaming methods, acoustic streaming control, such as

118   switching on and off, can occur instantly in comparison to hydrodynamic timescales. Further, acoustic

119   streaming is contactless and less sensitive to fluid viscosity, making it a versatile tool for creating an

120   exciting range of fluid motions. We choose ~80 MHz and ~200 MHz frequencies with wavelength (λ_s

121     $= C_s/f$) of ~50 μm and ~20 μm respectively, on the substrate ($C_{LiNbO_3} = 3980 \ [m/s]$)[50] as working

122   frequencies. (Table S.2) Upon attenuation into the liquid medium these frequencies remain constant

123   but due to slower speed of sound propagation through water ($C_{water} = 1498 \ [m/s]$)[50], the wavelengths

124   are reduced to about 7.5 μm and 15 μm, respectively. These wavelengths are in the range of a single

125   or small cluster of 2-3 cumulus cells (acting as Mie particles), resulting in higher force experience in a

126   standing wave configuration.[51,52] Further details on the acoustic induced fluid flow, attenuation

127   lengths, acoustic radiation force and drag force on particles are provided in the "SAW induced

128   acoustofluidic fields" section, Fig.2 and Table S2.

129

130   The acoustically active areas encompassed by the IDT pairs on the substrate are either $1 \times 1\ mm^2$ for

131   a 200 MHzdevice or $2.5 \times 2.5\ mm^2$ for an80 MHzdevice. In the case of the larger active area and

132   working frequency of $80\ MHz$, the IDT pairs reside outside of the fluid vessel and are excited in a dry

133   state while in the case of a smaller active area and working frequency of $200\ MHz$, a portion of IDTs

134   reside inside the fluid vessel and are excited inside the fluid in a wet state. (Fig.1C-D) The later usage

135   of IDTs inside the microwell also requires an extra passivation layer for IDT protection and the

136   prevention of inadvertent cell damage due to exposure to charge carriers via dielectrophoresis. No

137   suppression of the generated SAW was observed even at the higher conductivity level of the saline

138   solution in the absence of the passivation layer.[53] Although the dry state IDTs have less fabrication

139   complications and are easier for impedance matching, SAW attenuation is more significant due to its

140   contact with the PDMS microwell and viscous heating of the walls.[54] The IDTs in the x direction of

141   LiNbO$_3$ consist of 5 interleaving fingers with an aperture of 50λ which are backed by a reflector grating

142   of 300 shorted electrodes; while the orthogonal IDTs in the y direction only consist of 20 pairs of

143   interleaving electrodes with slightly different width and spacing from the x direction IDTs without any

144   reflector gratings. The slight difference in the IDT spacing in the x and y directions, and the narrower

145   resonance frequency bandwidth in the$x$direction, allow us to instantaneously switch the direction of

146   standing waves in the microwell cavity such that cells experience changes in the flow and agitation

147   patterns (Fig. 2C , Movie S1-S2). The acoustic streaming in the dry state device is created by the

148   attenuation of acoustic energy from the sound beam propagating inside the liquid in the microwell,[44]

149   while in the wet state device the waves are locally coupled with the fluid that covers the stimulating

150   transducers (Fig1. C_D).

151

152   Driving modalities employed in this study are shown in Fig1.E (i-iv). In the continuous wave (CW)

153   mode, the actuation frequency is set at the resonant frequency of the IDTs in the x direction while in

154   the frequency modulation mode (FM) the actuation frequency is switched between x and y direction

155   resonant frequencies at predetermined intervals of 2 seconds. In the pulse modulation mode (PM) the

156   resonant frequency of the IDTs in the x and y directions are pulsed at 1 KHz with 50% duty cycle for 2

157   second intervals. Lastly, the swept FM mode (SFM) consists of two chirp type excitions for x and y

158   direction resonant frequencies. We swept the frequency from $f^i_{resonant} - \Delta^i f^i$ to $f^i_{resonant} + \Delta^i f^i$ ($i = x,y$)

159   for a predetermined time interval of 2 seconds, alternating between resonant frequencies in each

160   direction. The sweeping bandwidths are determined from FWHM measured in each direction

161   independently.[55] We developed the last actuation scheme due to two reasons: first the quality factor of

162   the standing wave is impacted by medium loading which causes a resonant frequency shift; and

163   second, the dependency of resonant frequency on temperature and its unwanted shifts due to

164   acousto-thermal phenomena that resulted in inferior device performance efficiency.[56–58] (Fig. S3).
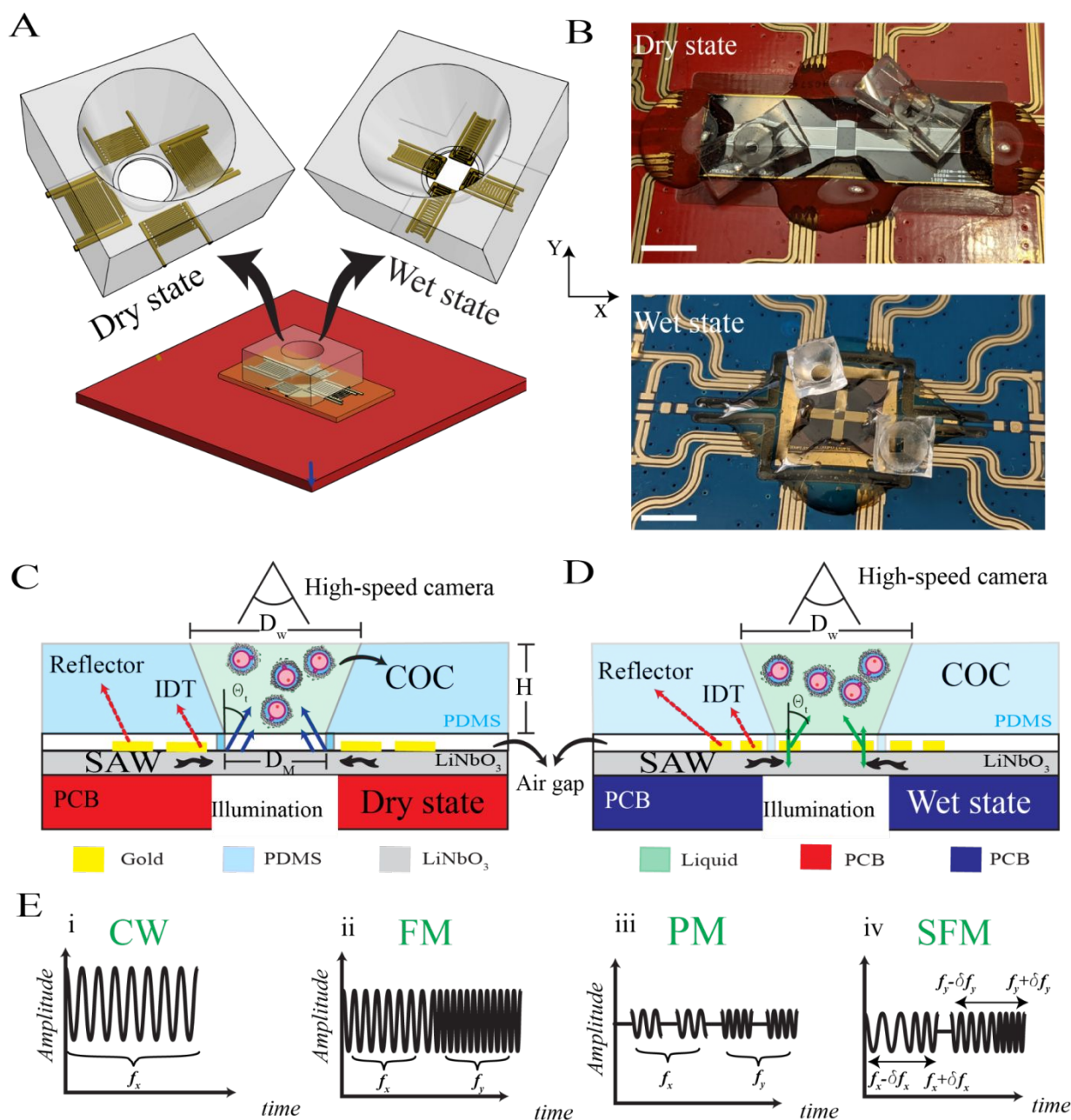
165
166 **Figure 1**. SAW based oocyte denudation module (A) schematic depicting the dry state (left) and wet state
167 (right) modes of denudation module including the configuration of IDTs used as SAW generators, and a
168 microwell that is located at the center of IDTs. (B) The photos of fabricated dry state device (top) and wet state
169 device with IDTs deposited on a 128° Y-cut LiNbO$_3$ substrate. Disposable microwells shown in both photos can
170 be reversibly bonded to the substrate for performing denudation procedure, X and Y shows the crystallographic
171 axes of the substrate. Scale bar is 1 cm. (C) Side view of the dry state denudation module showing the
172 configuration of IDTs in the periphery of the microwell located on top of the substrate and interaction of the
173 Traveling SAW with the fluid and cells inside the microwell. The Rayleigh waves interacting with fluid convert
174 into leaky Rayleigh waves that radiate into the liquid at the angle of θ$_t$. (D) Side view of the wet state denudation
175 module showing the configuration of IDTs submerged inside microwell located on top of the substrate and
176 interaction of the SAW with the fluid and cells inside the microwell. The Rayleigh waves are both directly
177 coupled with liquid and convert into leaky Rayleigh waves that radiate into the liquid at the angle of θ$_t$. (E)
178 Driving signal modalities employed for SAW generation. (i) Continuous wave (CW) (ii) Frequency modulated
179 (FM) (iii) Pulse modulation (PM) and (iv) swept frequency modulation (SFM). Modulated signal modes switch the
180 directions of dominant SAW propagating into the liquid at specified time intervals for achieving a complete
181 agitation.

SAW induced acoustofluidic fields

182

183   Upon applying a high amplitude 80 MHz CW excitation signal in the dry state devices (Fig. 2A(i-ii))

184   streamlines with four vortical structures appeared, despite the contact geometry of the microwell,

185   these concentrated the particles into a few vertical rings which are depicted schematically in Fig. 2D(i-

186   ii) and in Movie S3(a). A small population of particles was also trapped on the surface vortices that

187   formed on the fluid surface (Fig. S3). When we applied a high amplitude 200 MHz continuous signal

188   to wet mode devices, stronger fluid jets were generated inside the fluid that concentrated all the

189   particles into tightly formed vertical loops (Fig. 2A(iii), Movie S3.(c)). The flow behavior and resulting

190   patterns can be described in terms of damping length on substrate $x_s = 0.45 \lambda_s (\rho_s c_s)/(\rho_f c_f)$ [59] and

191   damping length in the water $x_f = 3\rho_s c_s^3/16\pi^2\eta f^2$ [60] (Table S.2). For both dry and wet devices, x_s is

192   smaller than the microwell contact diameter (D_M) this ensures that the generation of acoustic

193   streaming rather than particle accumulation on the lines associated with standing waves form inside

194   the fluid in the case where $x_s > D_M$. For the lower frequency dry state device, x_f (>10 mm) is larger

195   than the fluid height in the microwell. As such, the acoustofluidic field has minimal decay over the fluid

196   height and reflects back at the air-liquid interface. The recirculated flows launched from each IDT

197   interact with each other as well as the microwell boundaries, to create vertical vortices that stretch

198   from the center of the acoustic cavity to two flanks of the IDTs in the x direction (Fig. 2D(ii),E(ii)). For

199   the high frequency wet state device, the x_f is smaller than fluid height inside the microwell. Hence, the

200   acoustofluidic field dissipates before reflection at the air-liquid interface creating a gradient closer to

201   the microwell bottom, resulting in lower particle velocities near the fluid surface. (Movie S3.(c)-(d)) In

202   both devices, the drag force, $F_{drag} = 3\pi\eta d_p v \approx 10^{-8} - 10^{-9} N$, where v is the acoustic streaming

203   velocity [61] exerted on the suspended 90-100 μm polystyrene particles, is comparable to the acoustic

204   radiation force stemming from attenuation of sound waves $F_{rad} = \pi d_p^2 (I/4c) Y_p \approx 10^{-7} - 10^{-8}N,$

205   where I is acoustic intensity and Y_p is the acoustic radiation force function of the polystyrene

206   sphere [62–65]. As such, we suspect that the particle's motion in vertical loops consists of an outward

207   push of acoustic streaming and inward pull of acoustic radiation force. [60,61] Applying SFM modulated

208   single breaks these fixed symmetrical patterns and results in chaotic azimuthal recirculations as

209   shown in Figure 2B(i-iii). Interestingly, applying the SFM modulated signal to a microwell with elliptical

210   bottom geometry creates a poloidal flow with toroidal circulations forms as shown in Figure 2B(ii),

211   Movie S3.(b)).
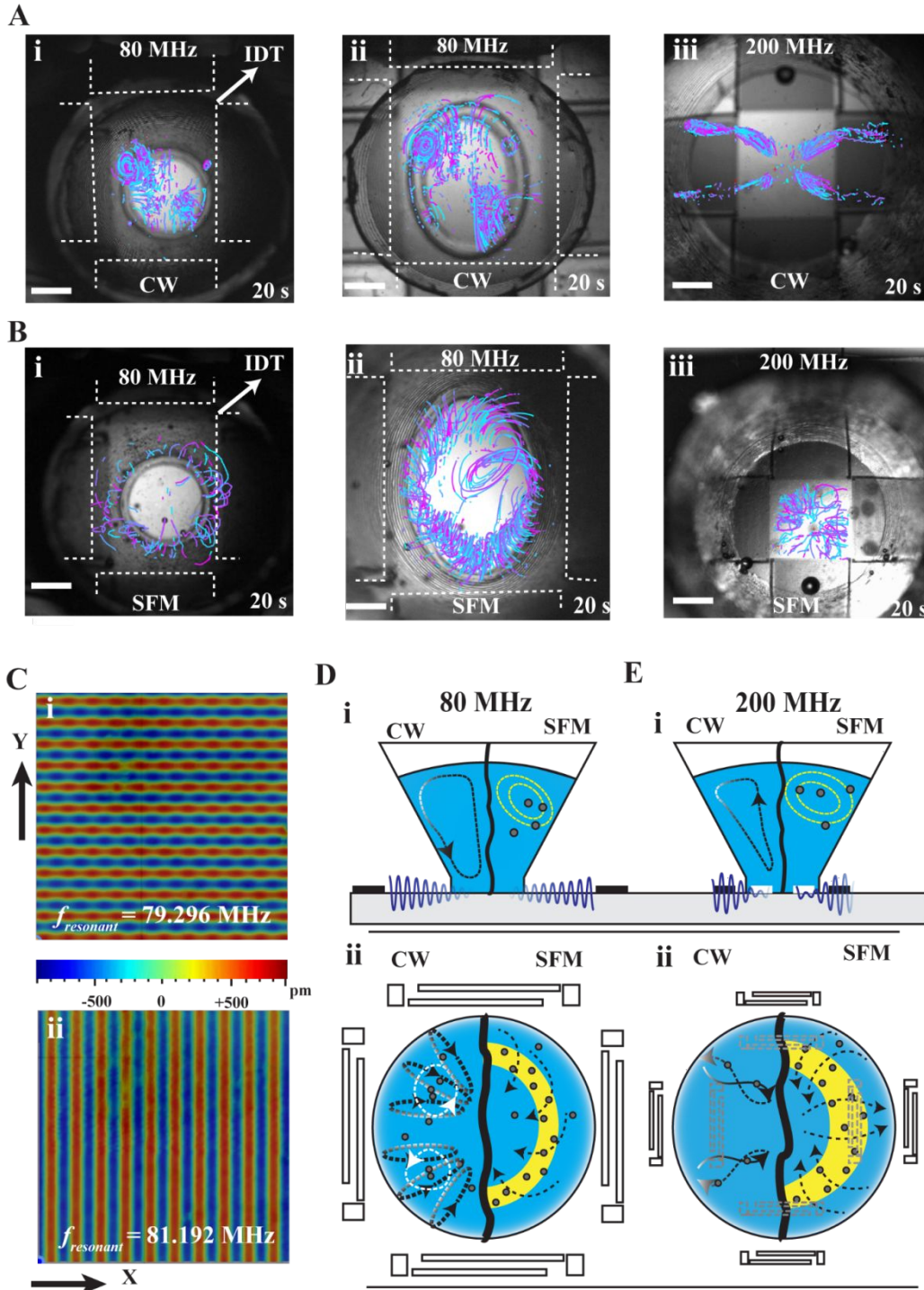
212
213   **Figure 2**. Mechanisms of particle and cell agitation. Representative particle/cell trajectory measurements for
214   CW and SFM driving signals using 15 and 90 micron particles. (A) The overlaid xy plane image of particle

215   trajectories, generated from particle tracking studies and stacked top view images when both devices were
216   actuated with a 20 dBm CW signal at x-direction resonant frequency. (B) overlaid xy plane image of particle
217   trajectories, generated from particle tracking studies and stacked top view images when both devices were
218   actuated with a 20 dBm SFM signal at 1 second intervals. (C) LDV measured data: SAW standing mode and the
219   uniformity switching between x direction (i) and y direction (ii). X and Y shows the crystallographic axes of the
220   substrate (D) Cross-section and top-down schematic illustration of internal streaming in the liquid filled
221   microwells of (i) dry state device for CW actuation and (ii) SFM actuation mode (E) Schematic illustration of
222   internal streaming in the liquid filled microwells of (i) wet state device for CW actuation and (ii) SFM actuation
223

Considerations for SAW intensity and dissipated energy

Acoustic intensity

226   Neither the diagnostic nor the therapeutic uses of ultrasound are unconditionally safe for use in

227   modern assisted reproductive medicine (ART).[39] Although the safety thresholds and operation

228   conditions have been being consistently examined, The exact effect of ultrasound output parameters

229   such as frequency, intensity, pulse duration and frequency that are used to drive the safety indices,

230   (i.e. Mechanical Index (MI), spatial-peak temporal-average intensity (I_{spta}), thermal index (TI)) on

231   biological matter is not completely understood.[37,66,67] Nonetheless, the mandated FDA thresholds in

232   the form of safety indices (I_{spta}, MI, TI), which convey the probability of ultrasound induced biological

233   effects is well accepted by medical community.[36] The majority of clinical ultrasound applications use

234   intensities between 0.03-1.0 W/cm^2, and it has been shown that intensities over 3000 mW/cm^2 can

235   have severe biological ramifications and may lead to cell apoptosis.[38,68,69] Further, MI<0.7 for bubble-

236   perfused tissue samples and MI<1.9 for samples without bubbles are the advised upper limitation for

237   safe ultrasound operation. The drive frequency, amplitude, modulation and exposure duration are the

238   major parameters contributing to the amount of energy impinging on the biological samples. [70,71]

239   Hence, development of ultrasound denudation protocols that assure lower intensity levels by at least

240   one order of magnitude is necessary to achieve a therapeutic outcome while remaining below the

241   toxicity threshold. [37,72]

242   The average acoustic intensity can be estimated from $\langle I \rangle = \frac{1}{T}\int_0^T p(t)\,v(t)\,dt$ where $p(t)$is the sound

243   pressure and $v(t)$is particle displacement. The transmitted pressure is a function of transmitted

244   particle displacement v as $|p_t| = \rho\,c\,\omega\,v$, where$\rho, c, \omega$ are the density, sound speed and angular

245   frequency, respectively. In our experiments, we measured the particle displacements of LiNbO$_3$

246   substrate in three conditions: unloaded, loaded with empty microwell, and loaded water filled

247   microwell as shown in Fig. 3.A, 3C. The intensity decay inside the medium can be further estimated

248   as $I = I_0 e^{-\alpha x}$where $\alpha = x_f^{-1}$is the absorption coefficient of ultrasound in water assuming close

249   compositional similarity of media with water (see Methods). Both dry and wet state devices can be

250   stimulated within the therapeutic window ($< 3000\ mW/cm^2$) which is close to recommended FDA

251   intensity levels for peripheral vessels and fetal ultrasound imaging (Fig. 3.B, 3D).[36,39,73] The worst-

252   case scenario analysis of the MI, considering the largest particle displacement and SFM mode of

253   actuation, also revealed that the MI of dry state and wet state devices are 0.0537 and 0.0849 (see

254   Methods) which are well within the recommended region (MI<0.7). It is important, however, to note

255   that the direct experimental measurement of acoustic intensities at these wavelengths is challenging,

256   and requires specialized hydrophones. Furthermore, the biological effects of a SAW on cell safety and

257   viability in chip scale levels may differ from the conventional culture dishes and are hard to model.[32]

258   Thus, we experimentally investigated the cell viability and development potential of mice embryos and

259   pups procured with our device and compared them to the control group of conventional artificial

260   insemination methods.
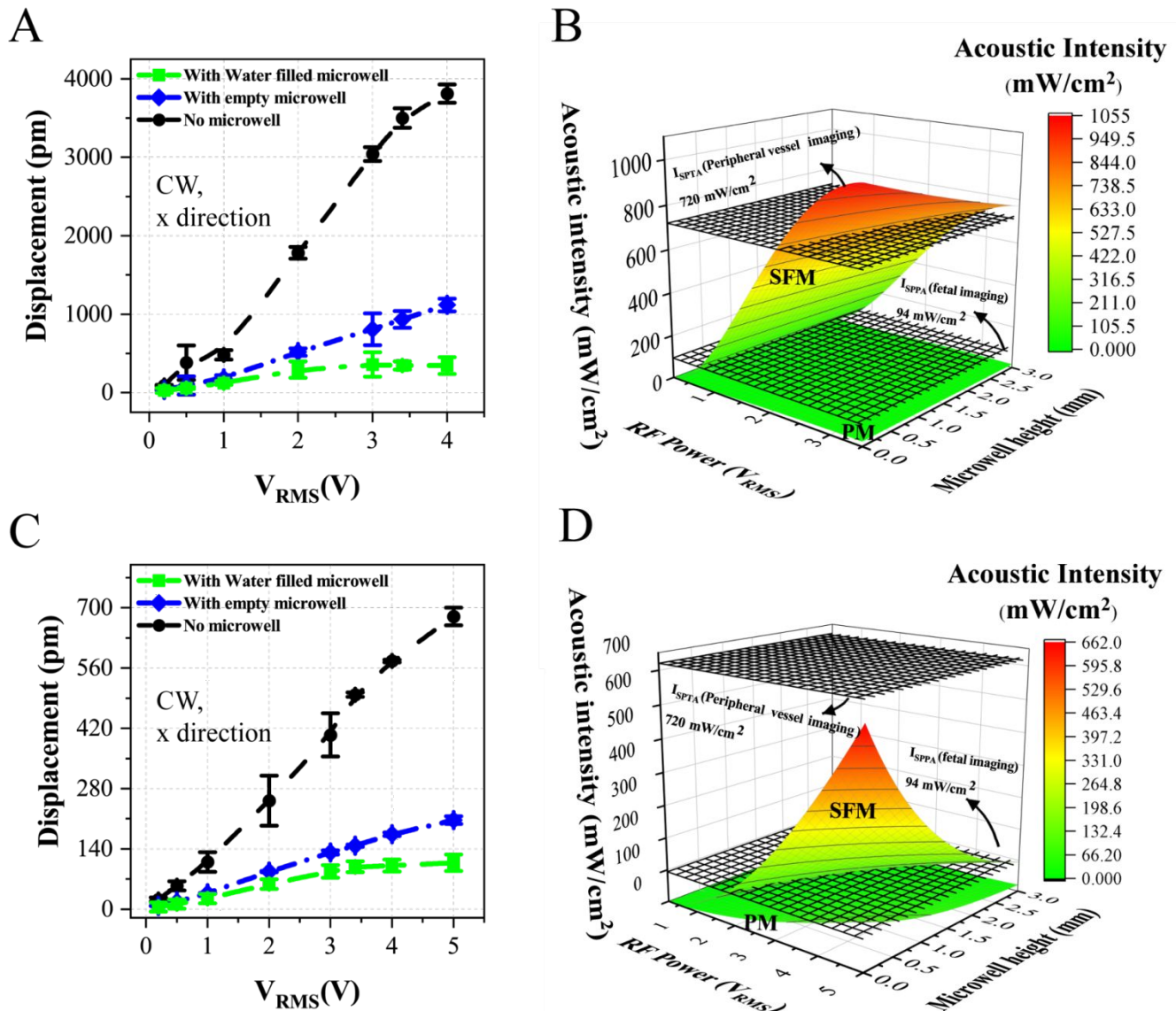
Figure 3. Displacement of the SAW on a bare LiNbO3 substrate (no microwell on top) (A) on the dry state device (C) on the wet state device. Acoustic wave intensity characterization using the LDV measured displacements for (B) the dry state device (D) the wet state device.

Ultrasound induced thermal effects

The rise in the temperature has always been a concern while using ultrasonics in screening of developing embryo/fetus due to the teratogenic effects of ultrasound induced hyperthermia.[74,75] As such, we investigated the acousto-thermal effect (energy conversion from acoustic to thermal) of our device for the denudation procedure. The viscous dissipation of acoustic energy is the main source of

271   generation of heat inside the liquid and the PDMS microwell. [42,76] Various insertion losses associated

272   with the generation of SAW, and Joule heating are the two other sources that may contribute to the

273   heat generation while performing a denudation procedure.[77,78] It is also important to note that $LiNbO_3$

274   is hysteresis free and in generating SAW it does not produce heat .[79] The Joule heating here is

275   related to the SAW accompanying electric field on the piezo substrate and solution electrical

276   conductivity. [77] We measured surface temperature variation of a bare $LiNbO_3$ substrate with a CW

277   signal at different driving powers after reaching a steady value (120 Sec) using a high sensitivity

278   infrared camera. Results shown in Fig. 4A are the spatial average temperatures in the acoustic cavity

279   (shown in the figure inset) for both the dry and wet state devices as a function of driving signal power

280   averaged over a 10 second period after 120 seconds of stimulation. In the worst case scenario after

281   applying a FM driving mode with power amplitude of $P = 3.5\ V_{rms}$ (corresponding to maximum

282   displacement of $\simeq 400\ pm$ in water) to a microwell filled with glycerol (a medium with high acoustic

283   absorption coefficient and low electric conductivity of $0.064\ \mu S/cm$), the temperature increased about

284   2.3 ℃ for the dry state device, and 1.8 ℃ for the wet state device, after 2 min with a time constant ($\square$)

285   of 11 seconds. The time constant is the elapsed time the device requires to reach ~67% of the final

286   steady state temperature indicating the dynamic behavior of the denudation device to a step input

287   function. In these experiments, electrical stimulation started after 30 seconds of thermal camera

288   recording initiation and switched off after one minute, followed by another minute of recording. After

289   switching off the power, the temperature returned to initial values with approximately the same time

290   constant. However, with PM driving signals (1 KHz, 50% duty cycle, 1 second intervals) the

291   temperature only increased 0.4 ℃ for the dry state device and 0.2 ℃ for the wet state device. The

292   dynamic temperature variation of M2 medium inside the microwells of both devices was also

293   measured and the results are shown in Fig. 4B representing the denudation protocols using both

294   devices. Further experiments also indicate that the coexisting electric field plays an important role in

295   acoustic induced heating through the Joule heating mechanism which can be alleviated by active

296   cooling of the substrates (see Methods)

297

298   Conceivably, temperature can modulate enzyme activity through reversible perturbation of protein

299   structures among other various mechanisms.[6] Considering that hyaluronidase (HA) is catalyzing a

300   chemical reaction that is happening on the surface of the cumulus cells, the small temperature

301   increase on the cell surfaces, due to higher absorption coefficient in comparison to medium ($Z \approx$

302    $1.55 \times 10^6 kg/m^2/s$ in soft biological tissue),[80] can act as a thermal driving force assuming Michaelis–

303   Menten kinetics under non-isothermal conditions while neglecting the effect of temperature on

304   reaction kinetic coefficients. This phenomenon can be further coupled to the chemical driving force,

305   reinforcing the reaction rate.[81] In sum, the temperature increase for most of the experiments used for

306   the denudation of fresh COCs remains lower than 2 °C, well below the recommended safety

307   temperature increase limit (thermal index of 6) in ultrasonic diagnostics.[78]

308
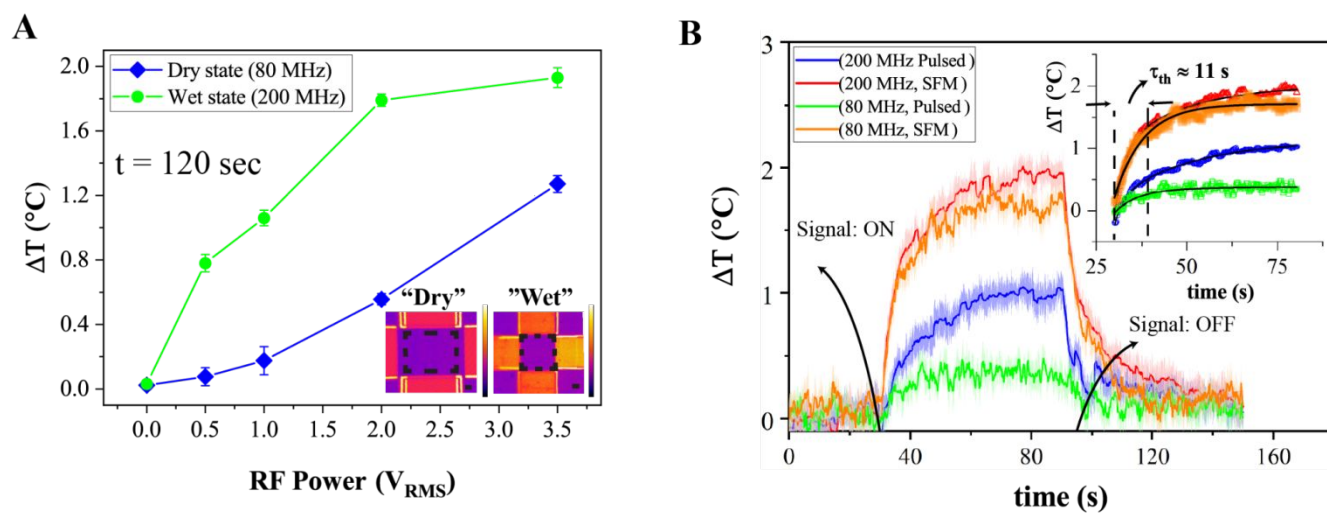
309

310   **Figure 4**. (A) Mean ± s.e.m temperature variation from room temperature of the acoustic cavities (see figure
311   inset) of dry and wet state devices without microwell as a function of input power (n=5 measurements), the
312   dashed squares shows the measuring areas (B) Ultrasound thermal effects, i.e. the difference of temperature
313   after ultrasound stimulation and biological temperature (37 °C) on the M2 medium filling the microwell for both
314   2.2 Vrms SFM and PM driving modes. Figure inset shows the time constant the temperature reaches 67% of the
315   stable temperature after 60 seconds.

316   ## Decoupling electrical effects in denudation procedure

317   The propagating surface acoustic waves created by the reverse piezoelectric effect (conversion of

318   electrical energy to mechanical displacement) create dynamic electric fields in the free area between

1

319   the IDT transducers by piezoelectric effect (conversion of mechanical energy to electrical energy).

320   Qualitatively, surface acoustic displacements cause surface charges through the piezoelectric effect;

321   the additional attraction between the surface charges causes additional strain, further stiffening the

322   substrate and increasing the surface acoustic wave velocity. [82] Hence, the coexisting electric field with

323   the surface acoustic wave can induce electrical stimulation and dielectrophoresis effects.[83] It has also

324   been shown that high frequency sinusoidal electrical stimulation (above 100 KHz) can alter the

325   dynamics in excitable cells, block ion channels and lead to electrical quiescence.[84] Furthermore, It has

326   been indicated in the literature that high SAW undulatory displacements ($\cong$ 10 nm, 10 MHz and power$\gtrsim$10

327   V_{rms}) can locally accumulate charges sufficient to create a half wavelength "nano-electrochemical" cell

328   that may split water and create free radicals.[85] As such, it is important to understand and identify the

329   sources of electrical fields that may affect the performance of the device. Two main sources of

330   unwanted electrical fields in our experimental design can be either through parasitic electric signal

331   coupling from wire bonds, or electrical fields associated with SAW. Depending on the conductivity of

332   the medium on top of the substrate, mirror charges can form which potentially decrease the strain and

333   velocity of the surface wave. The conductivity of the culture medium is $19\ \mu S.cm^{-1}$(856

334   conductometer module, Metrohm, Herisau, Switzerland) which significantly lowers the electric field

335   vector inside the medium and thus lowers any dielectrophoresis forces. In addition, the electric field

336   exponentially decreases with distance from the bottom of the substrates. As such it is safe to assume

337   that cells being agitated a small distance from the substrate are not exposed to any SAW mediated

338   electric fields. For confirming this hypothesis, we used 1 μm polystyrene particles dispersed both in

339   deionized water and M2 solution and exposed them to CW mode acoustic agitation at 24 dBm. The

340   similarly assembled clusters of particles in both deionized water (low electrical conductivity) and M2

341   culture (higher electrical conductivity) medium indicate the acoustic field has the main mechanism of

342   particle trapment. For further confirmation, we drove the 80 MHz acoustic module at off resonant

343   frequencies of 30 Mhz, and 150 MHz with higher RF power of 30 dBm (Fig. S4). Under these

344   conditions, of weak electromechanical coupling and imperceptible SAW coupling in the fluid, we did

345   not observe any microbead assembly. This evidence also confirms the absence of parasitic electric

346   fields (wire bonding, PCB board etc). Finally, for electromechanical coupling conservation in the wet

347   state device with the immersed IDTs inside the microwell, the substrate surfaces were shielded with

348   either a self-assembled monolayer (SAM) film of trichlorosilane [53] or a thin layer of silicon dioxide.

349   Denudation efficiency

350   We investigated the performance of each device and examined device-to-device variability by

351   following the frozen COC denudation protocol in two different devices for both the wet and the dry

352   modules. We optimized three parameters: driving modality; power; and exposure time for achieving a

353   complete denudation in the safest yet most efficient way. First, to compare the three driving conditions

354   and device performance, we chose, based on intensity measurements, $20\ dB_m$ ($2.236\ V_{rms}$) as the

355   working RF power and a 90 second exposure time. It is important to note that using different actuation

356   modalities, even using the same driving power, results in different intensities. For the dry state

357   module, the CW, PM, and SFM modes of actuation yielded a mean denudation efficiency of 93.8%,

358   90.7% and 94.6% respectively for device-1 compared to a mean denudation efficiency of 95%, 90.2%

359   and 96.8% respectively for device-2 (Figure 5A). Denudation efficiency is defined as the ratio of (

360    $A_{untreated} - A_{treated})/A_{untreated}$, where A in the area of cumulus cells, determined through image

361   processing of the phased contrast images taken of the oocytes before and after the procedure

362   (Fig.S2) . It is worth noting that the yield of the device, as in recovery of whole oocytes, can be

363   considered 100% excluding oocyte loss due to human error during transfer steps. Similarly, for the

364   wet state module, the CW, PM and SFM mode of actuation resulted in 94.8%,87.8%,and 92.4%

365   denudation efficiency for device-1 which are comparable to 94%, 88.8%, 96.2% denudation efficiency

366   of device-2. Two way ANOVA analysis indicate that at level 0.05 the population means of frequency

367   factor are not significantly different (p =0.36) but at level 0.05, the population means of actuation

368   modes (CW, PM, SFM) are significantly different (p= 8.9E-4). Fig.5B-C shows a representative result

369   of the SFM mode denudation procedure using the aforementioned parameters. We chose SFM mode

1

370   of actuation as the most effective mode of actuation and optimized the power and exposure time

371   consequently.
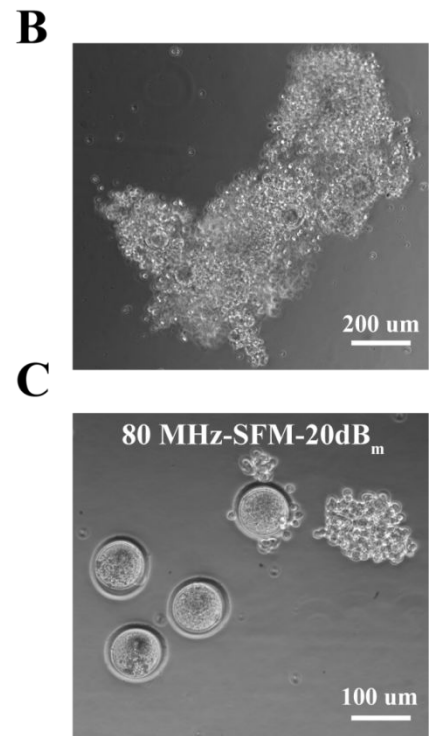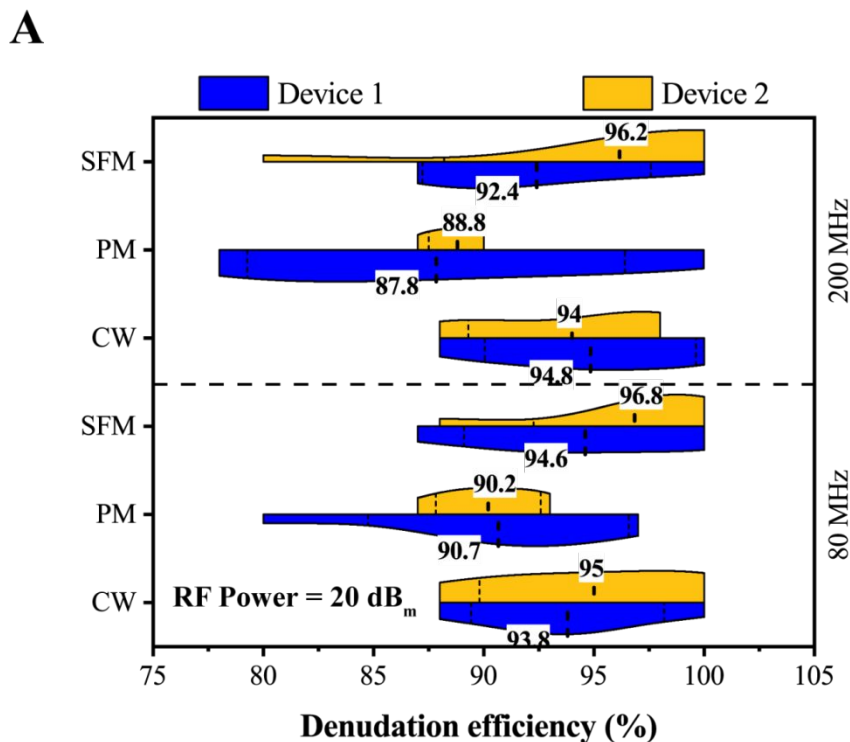
372
373   Figure 5. (A) Denudation efficiency as a function of device mode, frequency and driving signal modulation. (B) A
374   compact cluster of MII stage COC before any chemical (HA) or mechanical treatment. (C) A few completely or
375   partially denuded oocytes retrieved from a dry state device operating at 80 MHz with a 20 dB$_m$ and SFM signal.

Effect of actuation power, and exposure time

377   The driving stimulation power (amplitude) and exposure time are the two main parameters that

378   determine the amount of energy inserted into a sample. For comparing the effect of power on the

379   denudation efficiency, we used driving stimulation powers of 15 dB_m (1.257 V_{rms}), 19 dB_m (1.993 V_{rms}),

380   and 24 dB_m (3.544 V_{rms}) for a 60 s exposure time. As expected the denudation efficiency increases

381   with increasing driving power for both devices as shown in Fig 6.A. This is due to the larger shear

382   stress that cells experience due to the higher acoustofluidic flow at higher power. From the particle

383   velocity measurements, the drag and acoustofluidic forces are approximately three times higher when

384   using the highest driving stimulation in comparison to the lowest level. This is expected as the total

385   force acting on the body of the fluid is assumed to have a linear relationship with the acoustic power

386   (see supplementary notes). Furthermore, the mean denudation efficiency also indicates a linear

1

387   relationship with applied stimulation power. We can infer then that the denudation efficiency is a

388   function of the drag force intensity which has a linear relationship with acoustic streaming magnitude.

389   Consequently, we chose $22\ dB_m$ ($2.815\ V_{rms}$) as driving power and investigated the effects of

390   exposure time. As shown in <u>Fig 6.B</u> the denudation efficiency also increases with exposure time

391   because of the extended chance of uniform exposure of all sides of the oocyte to shear stresses.

392   From exposure time experiments we realized that as the time of exposure increases, oocytes are

393   more uniformly denuded in comparison to applying higher driving forces in shorter time periods.

394   Representative images of partially denuded and completely denuded COCs using the ultrasound

395   devices are shown in <u>Fig. 6C(i-iv)</u>. (Pearson correlation tests reveal a statistically significant

396   correlation between the power level and denudation efficiency for both dry and wet state modules (P

397   value = 0.011 and P value = 0.043 respectively) as well as denudation period and denudation

398   efficiency for both dry and wet state modules (P value = 0.045 and P value = 0.038 respectively). In all

399   cases the correlation coefficients are r >95%. However, a two-tail student test shows no significant

400   difference between wet and dry state modules for denudation procedure given either individual

401   operating conditions or collective conditions. (p-value = 0.79 and p-value = 0.82 for power and

402   denudation period respectively). As mentioned previously, the biological effects of SAW on cells in

403   miniaturized experiments is very hard to model and predict. As such, we carried out artificial

404   insemination experiments to directly investigate the impact of ultrasound on the development potential

405   of mice oocytes.
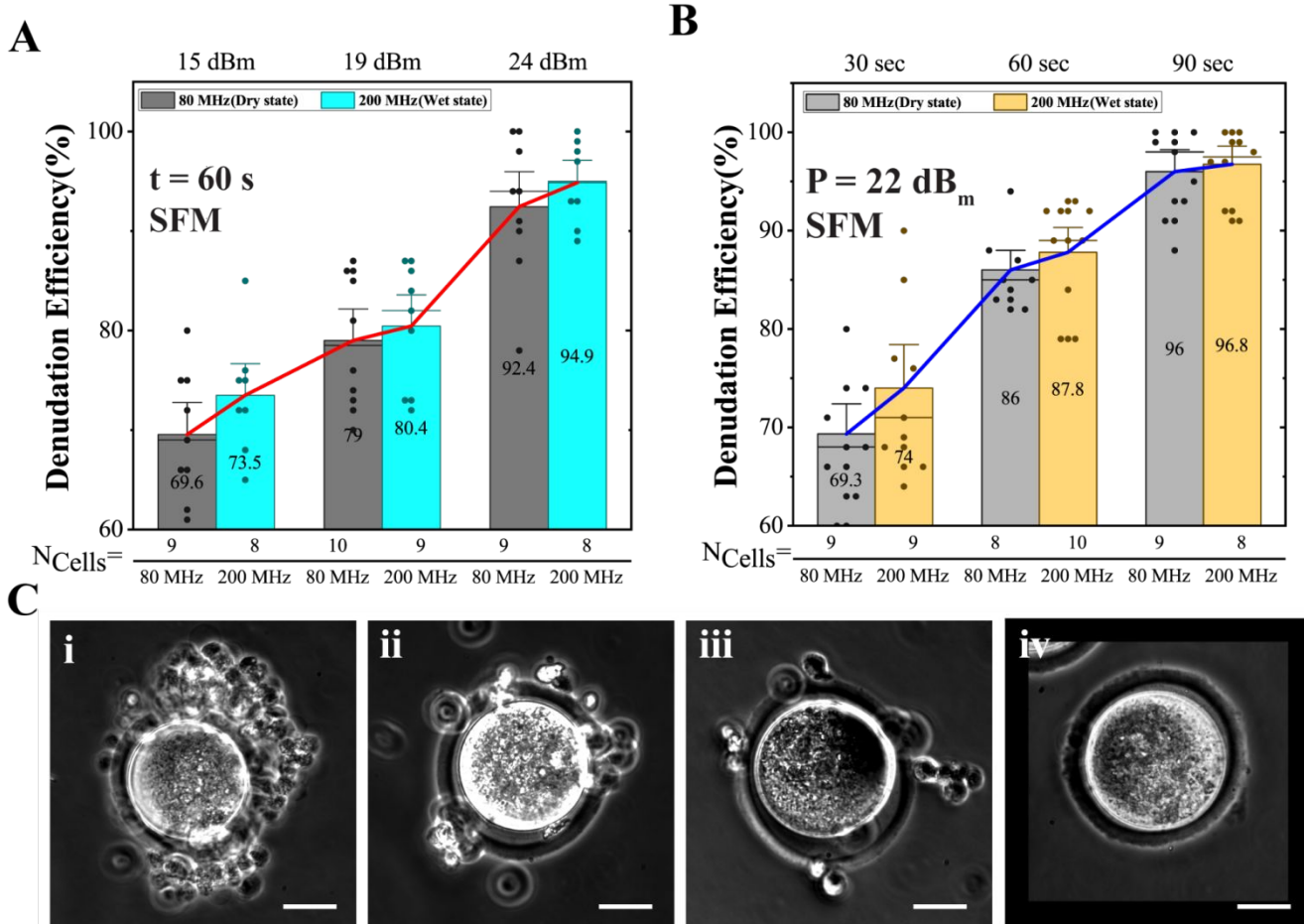
406
407 Figure 6. (A) The effect of SAW power on denudation efficiency for both devices using an SFM sigal and 60
408 second exposure period.There exist a significant correlation between power level and denudation efficiency for
409 both dry state (P value <0.05) and wet state (P value <0.05) modules ((B) The effect of exposure time on
410 denudation efficiency of both devices using a 22 dB_m SFM signal.There exist a significant correlation between
411 power level and denudation efficiency for both dry state (P value <0.05) and wet state (P value <0.05) modules.
412 There is no significant difference between dry and wet state modules for performing denudation given the
413 current operating conditions. (C) Representative images of partially denuded and completely denuded
414 COCs using the ultrasound devices

Fertilization and Development potential of ultrasonic denuded oocytes

416 To test the efficiency and safety of the device, 40 oocytes denuded by 80 MHz SAWs, 25 oocytes

417 denuded by 200 MHz SAWs, and 30 oocytes denuded by manual protocol (MP) serving as control

418 were inseminated by piezo-actuated ICSI. The device significantly reduced the labor of the process,

419 and the denudation quality remained the same without any oocyte loss. After piezo-actuated ICSI, the

420 80-MHz, 200-MHz, and MP groups yielded comparable survival rates of 82.5%, 84.0% and 83.3%

421 (P=0.96), respectively. Fertilization rates were also comparable between the three groups at 80.0%,

2

422   80.0%, and 83.3% (P=0.88), respectively, as well as blastulation rates of 72.5% vs. 72.0% vs. 66.7%

423   (P=0.69), respectively (Fig. 7). After reviewing embryo development in the time-lapse imaging system,

424   all three groups had similar morphokinetics with no incidence of extensive embryo fragmentation or

425   abnormal cleavage (Table.S1). After transferring the resulting blastocysts into recipient mice, 9 live

426   births were achieved from the 80-MHz group, while 5 were achieved from the 200-MHz group

427   (Table.1). All pups were weaned to date without compromised development and are fertile. (Movie

428   S7)
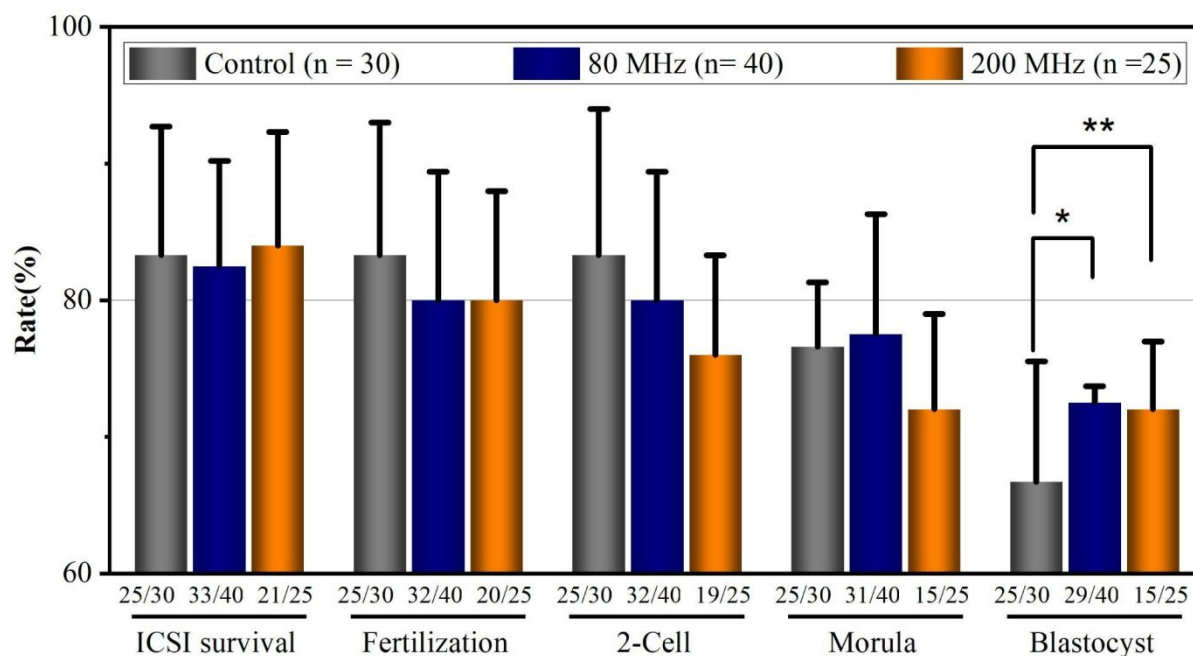
429

430   Figure 7. Overall ICSI Micromanipulation survival and Embryo Development Data (mean and SD).
431   Control is manual protocol (MP). *P value >0.1 and **P value>0.1 indicate a comparable blastocyst
432   rate between control, dry state and wet state modules.
433

434

435

436

437

438

439

440

2

441   Table 1. Embryo Transfer and Pregnancy Outcomes

	Total Blastocysts Transferred	Number of total recipients	Number of pregnant recipients	Born	Alive	Average Birth Weight (g)	Weaned
Control	20	2	2	8	8	1.58 ± 0.41	8
80 Mhz	29	3	3	10	9	1.62 ± 0.36	9
200 Mhz	15	2	2	5	5	1.60 ± 0.11	5

442

Conclusion and Outlook

444   In this study, we developed a contactless 3D cell agitation platform for oocyte denudation by

445   reshaping 2D SAW wave fields inside a biocompatible microwell, by modulating excitation signals. We

446   investigated the flow patterns, potential denudation mechanisms and safety of our developed devices.

447   The arrangement of IDTs, small differences in IDT spacing, and reflector grating use in one direction,

448   provided us with an efficient method to switch the flow inside the microwell by modulating only the

449   excitation signals.The signal modulation is also used for controlling and keeping the acoustic intensity

450   within the recommended FDA limits for peripheral vessels and obstetrical and gynecological imaging.

451

452   With the current experimental design, we are able to carry out up to 30 oocyte denudation in less than

453   3 minutes which significantly improved the procedure efficiency and reproducibility while minimizing

454   enzymatic treatment and reducing the out-of-incubator time. The safety of this device is validated by

455   normal embryonic morphokinetics and live births from the mouse oocytes denuded in this study.

456

457   The simple design and straightforward setup of our device in combination with low power density

458   requirements indicate that our technique is an efficient and safe method for preparation of oocytes for

459   ICSI procedures. Our technique also has the potential to be modified and integrated with a small RF

460   supply with simple electronics. This will allow it to function as a portable, inexpensive, and automated

2

461   device that yields reproducible results and expands the reach of ICSI procedures in places without a

462   sufficient number of highly skilled embryologists or large well-endowed laboratories, thus reducing

463   costs overall.

464

465   Our future research includes computational modeling to elucidate the details of the mechanism of

466   action. In addition, further and detailed investigations of ultrasonic effects on human gametes

467   including cellular restructuring, mechanosensitive ion channel activity, differentiation, toxicity, and long

468   term development are in progress. Lastly, this work validates the potential of an automated

469   embryology lab-on-a-chip device for the denudation of oocytes.

Methods

470

Device fabrication

471

472   Fabrication of the ultrasound denudation module consists of two major parts. First, the deposition of

473   IDTs on the lithium niobate and fixation of the wire bonds to the PCB using potting epoxy. Second, the

474   fabrication of microwells that sit on top of the $LiNbO_3$ substrate. The details of the manufacturing

475   process of both steps are discussed in <u>supplementary notes</u>.

476

Driving Stimulation Modes and Acoustic Field Intensity Calculations

477

478   We calculated the intensities for the worst case scenario of maximum particle displacement without

479   any decay throughout the microwell-substrate contact area. Acoustic intensity for SFM mode can be

480   estimated from $I_{SPTA}^{SFM} = \frac{1}{t_2 - t_1} I_m \int_{t_1}^{t_2} \left(\frac{p_{env}(t)}{p_m} \right)^2 dt$ where integration period chosen to be over the time of

481   frequency sweeping (2 seconds), $I_m = p_m^2/2\rho c$ is the maximum intensity and p_{env} is the envelope of

482   the swept pressure assuming a normal distribution of particle displacement as a function of frequency

2

483   sweep. For the PM mode, we estimated the intensity from $I_{SPPA}^{PM} = f_p I_m \int^{PD} \left(\frac{p_{env}(t)}{p_m} \right)^2 dt$ where f_p is pulse

484   frequency repetition $(1\ KHz)$ and integral is over a single pulse $(PD = 500\ us)$. Finally, we calculated

485   the mechanical index from $MI = p_{r.3}(z_{SP})/(f_c^{1/2})$ in which the $p_{r.3}$ is the the peak rarefactional pressure

486   in megapascals (MPa) derated by 0.3 dB/cm-MHz and f_c is the center frequency in megahertz (MHz).

487   We used an Anritsu (MG3960C) RF/Microwave signal generator to address the signal modulation

488   requirements. The single port driving signal is then splitted by a 4 way power splitter (Mini-Circuits,

489   ZFSC-4-1W-S+) connected to 4 input ports of the device.

490

491   Finally the chirp signals in SFM mode refers to sinusoidal signals that their frequency is a function of

492   time without any amplitude modulation that can be applied further on the signals. In a predetermined

493   time period we sweep the frequency from an minimum value $(f_{Amplitude/2})$ to a maximum value (

494    $f_{Amplitude/2}$) with a constant amplitude which can be mathematically represented by $s(t) = w(t)sin(2\pi$

495    $f_0 t + \pi B t^2 / T)$ in which $w(t)$ is the amplitude rectangular window of width T, B is the chirp width and f_0 is

496   the starting frequency. [55]

Ultrasound denudations protocols with Frozen and Fresh COCs

498   For *in vitro* performance evaluation and parameter optimization, we tested our devices with frozen

499   COCs. Frozen straws containing 5 intact COCs were thawed in a petri dish according to provided

500   protocols. We used a 1 mm in diameter transfer pipette tips to avoid any manual denudation during

501   the washing and transferring steps. After complete rehydration, we transferred the COCs into the

502   microwell containing thermally equilibrated EmbroyMax M2 Medium with Phenol Red & Hyaluronidase

503   (M2+HA) product number MR-051 from Sigma-Aldrich. Immediately after transferring the solution to

504   the microwells, the samples were treated with ultrasound per one of the driving modalities. After the

505   procedure, we transferred the denuded cells to a droplet on a petri dish and acquired phase-contrast

506   images for denudation efficiency assessment and quantification (Fig. S1A, Movie S4).

507

508   For in vivo testing, fresh COCs were retrieved from the oviducts of hyperstimulated B6D2F1 mice.

509   The clusters of COCs were then mechanically isolated into individual COCs. The COCs were then

510   allocated for denudation by either SAW or by conventional manual pipetting aided by hyaluronidase

511   similar to in vitro protocol. Piezo-ICSI was performed on denuded oocytes, and post-ICSI oocytes

512   were cultured and monitored in a time-lapse incubator up to 96h. Blastocysts were transferred into

513   pseudo-pregnant 2.5 dpc CD-1 surrogates. The pregnancy, delivery, and health of pups were

514   assessed (Fig.S1B, Movie S5-S6).

515   Image segmentation

516   Analyzing 2D images of COCs during or after the denudation procedure is a challenging and

517   cumbersome task. This is mainly because of significant inhomogeneity in the background and

518   foreground intensities of the images. During the denudation, the cumulus cells accumulate inside the

519   microwell and remain in close vicinity to the oocyte. The oocytes' movements inside the microwell

520   also have a vertical component that quickly pushes them out of focus of the camera. Despite labeling

521   hundreds of images extracted from the acquired Movies and training several convolutional neural

522   networks (CNNs) mainly with a U-shape structure (U-Net), we were unable to produce a robust CNN

523   model to predict denudation efficiency. Consequently, for consistent images and preventing

524   tediousness of training new CNNs, we first acquired cell images in a droplet with a phase-contrast

525   microscope after extracting cells from the microwell. And second, we adapted to use an unsupervised

526   image segmentation method based on non-separable wavelets similar to those recently developed for

527   gel electrophoresis image analysis.[86,87] The details of the image segmentation method and

528   implementation code can be found in work of Sengar et al.[87–89] The image processing workflow is as

529   follows: (1) The original images are normalized between 0-1. (2) The normalized images are

530   decomposed using an undecimated non-separable quincunx wavelet to obtain same size

531   decompositions for better comparison. (3) A linear minimum mean squared error estimation (LMMSE)

532   based noise filtering method is applied on wavelet coefficients to capture all the singularities and

533   noise. (4) The texture characterization and spot detection followed by an edge detection is performed

534   in the wavelet domain to define the local textures. (5) The overlapped spots and regions of thin

535   streaks and noise are further refined by using a morphological opening operation using a disk shape

536   structure with similar diameter of a single cumulus cell (10 microns). (6) The minimum energy regions

537   are determined to remove all the edges that do not fall under this criteria as well as supersaturated

538   spots in the image. (7) The results of previous steps are merged to render the final segmented image.

539   To capture all the areas associated with the cumulus complex, all the steps are repeated twice for two

540   different scenarios of segmenting darker and brighter regions (Fig. S1.Aii-Dii and S1.Aiii-Diii). Due to

541   texture similarities of cumulus cells with zona pellucida, and oocyte cytoplasmic regions, this method

542   also detects cytoplasmic regions as cumulus cells. As such, the final segmentation is followed by

543   detecting the cytoplasmic region using the Hough transform algorithm. Lastly, the resulting masks of

544   detecting darker regions, brighter regions, and oocyte cytoplasm are merged together to produce the

545   final segmentation mask (Fig. 1S.Aiv-Div.)

546

547   To calculate the denudation efficiency, the untreated COC cumulus area is defined as the average of

548   five calculated areas from 2D images of individual intact COCs. Furthermore, the residue areas

549   remaining on treated oocytes is calculated as the difference between the calculated area of treated

550   oocytes with average area of at least five completely denuded oocytes.

551

552   It is worth mentioning that the image analysis method is only a partial representation of denudation

553   efficiency. The cumulus cells are attached at all of the oocyte surfaces in 3D and a 2D image

554   segmentation cannot capture all of them. Another weakness of these methods is that it is sensitive to

555   image quality and size inhomogeneities of cells. In case of very small, very large, or fragmented

556   oocytes the calculated denudation efficiency can result in non-logical values that should be either

557   handled manually or be discarded as outliers. In addition, this image analysis method is only used for

558   quantification, and optimization of parameters for in vitro protocol. In the experiments with fresh

559   COCs, the procedure is more dynamic. An experienced operator accesses the oocyte denudation

560   progress visually by pausing the procedure. In case of complete denudation, he stops the procedure

561   and extracts the cells, otherwise he resumes the procedure to achieve complete denudation. (Movies

562   S5)

Measurement and estimation of ultrasound induced thermal

563

dissipation

564

565   We measured the acoustic induced temperature variations with an infrared camera equipped with a

566   high sensitivity magnifying thermal lens (T300 FLIR systems). We used a hotplate to calibrate the

567   emissivity of measurements for $LiNbO_3$, M2 and glycerol mediums used in the measurements.

568   Temperature measurements were first carried out at the surface of the substrate respectively in

569   droplets of deionized water, M2 medium and glycerol on top of a $LiNbO_3$ substrate. The temperature

570   increase on the surface of the substrate can only be attributed to power dissipation of the SAW

571   resonators[90] while measurements in droplets give indications of both acoustic absorption and joule

572   heating. Further experiments also revealed that the temperature increase could be controlled by the

573   power of the driving mode, pulse duration, PRF similar to diagnostic ultrasound, and active cooling of

574   the substrate.

575

576   The temperature increase solely due to complete acoustic absorption can be theoretically estimated

577   according to $\Delta T = Q'\Delta t/\rho C_p$ where Q' is ultrasound generated heat flux, t is stimulation duration, C_p is

578   specific heat capacity of medium and ρ is medium density.[72,80] The ultrasound generated heat also can

579   be calculated from $Q' = \alpha P^2/\rho c$ where P is effective pressure and α is the absorption coefficient. The

580   temperature increase for alternating electric fields below 300 MHz can be also estimated from $\nabla \cdot (k_m$

581   $\nabla T) + \sigma E^2$ where k_m is thermal conductivity of medium, σ is electrical conductivity of the electrolyte

582   and E is the electric field vector.[77] Temperature rise in deionized water following theoretical estimation

583   for CW ultrasound after 2 minutes is 1.8 $°C$ which is higher than the experimentally measured

584 temperature. The difference can be attributed to several factors such as inaccurate estimation of

585 acoustic absorption, neglecting evaporation, or heat convection due to acoustic streaming. Also,

586 temperature measurements using cell culture medium shows that higher conductivity mediums

587 enhance the Joule heating contribution in comparison to deionized water. Also, considering very low

588 electric conductivity of glycerol, the temperature increase in the glycerol indicates the dominance of

589 acoustic absorption in medium over Joule heating.

590 Animal use and Acquisition of gametes

591 For initial tests and optimization steps, we used commercially available cryopreserved metaphase II

592 mouse (B6C3F1) oocytes (Embryotech Laboratories Inc. USA) [91] with intact cumulus cells.

593 To obtain oocytes for in vivo experiment, 12-week-old B6D2F1 female mice were injected

594 intraperitoneally with 0.2 ml of pregnant mare serum gonadotropin and inhibin cocktail (CARD

595 Hyperova, Cosmo Bio, Japan) for ovarian hyperstimulation. After 48 hours, 7.5 IU of human chorionic

596 gonadotropin (hCG, CG10, Sigma-Aldrich, Saint Louis, MO, USA) were administered to trigger

597 ovulation. About 16 hours post hCG trigger, the mice were euthanized by cervical dislocation. The

598 oviducts were surgically removed and transported to the micromanipulation lab in potassium-

599 supplemented simplex optimised medium (KSOM) media (CARD KSOM, Cosmo Bio. Japan). The

600 ampullae were punctured by a 30 gauge needle to release the COC cluster into clean KSOM media

601 droplets and allocated for manual pipetting or SAW denudation.

602

603 To obtain spermatozoa, the cauda epididymis of 10-week-old B6D2F1 male mice were retrieved

604 surgically and transported in human tubal fluid medium (HTF, Irvine Scientific, Santa Ana, CA, USA).

605 The spermatozoa were released into a clean HTF medium droplet by microdissection. The

606 spermatozoa were incubated in 37°C, 5% CO_2 and 92% humidity for 3 hours minimum prior to use for

607 ICSI. The concentration of spermatozoa was adjusted to achieve a final concentration of 3 million/mL

608 for piezo-ICSI.

609

610 All B6D2F1 mice were obtained from Jackson Laboratory (Bar Harbor, ME, USA). All CD-1 mice were

611 purchased from Charles River Laboratories (Catskill, NY, USA). All animal treatments were approved

612 by the Institutional Animal Care and Use Committee of Weill Cornell Medicine.

613 ## ICSI Procedure

614 Piezo-actuated ICSI was performed based on previous protocols with slight adjustments.[92] A blunt

615 injection pipette (Piezo Drill Tip ICSI, Eppendorf, Germany) was back-loaded with Fluorinert (FC-770,

616 Sigma-Aldrich, Saint Louis, MO, USA) and attached to micropipette holder equipped with piezo

617 actuator (PMM-150FU Piezo Impact Drive, Prime Tech, Japan or PiezoDrill, Burleigh, Victor, NY,

618 USA). A mineral oil covered micromanipulation dish was prepared. Spermatozoa were loaded into the

619 center PVP droplet and up to 10 oocytes were transferred in each surrounding M2 media (CARD M2,

620 Cosmo Bio. Japan) droplet for the ICSI procedure.

621

622 To prepare the injection pipette, residual air and a small quantity of Fluorinert were expelled into a

623 PVP droplet. The injection pipette was then primed by suctioning PVP until smooth control of the

624 Fluorinert-PVP meniscus was obtained . Mouse sperm heads were mechanically separated and

625 aspirated into the injection pipette. While securing a single oocyte at 9 o'clock by the holding pipette

626 (Custom made holding pipettes, Hamilton Thorne, Beverly, MA, USA), a laser (LYKOS, Hamilton

627 Thorne, Beverly, MA, USA) is applied to the zona pellucida to create a breach, the injection pipette

628 was then inserted through the breach, and advanced through 80% of the oocyte forming an

629 invagination. A weak piezo pulse was applied to breach the membrane and deposit the sperm head

630 into the ooplasm. The pipette was retracted while aspirating gently to close the oolemma to avoid

631 degeneration. Alternatively, the zona could be breached by applying a stronger piezo pulse without

632 the assistance of a laser. (Movie S8)

Embryo Culture, Embryo Transfer and Pregnancy Outcomes

After ICSI, oocytes were washed thrice in KSOM media before transferring into the time-lapse

incubator. A single oocyte was loaded in a microwell in EmbryoSlides (EmbryoSlide, Vitrolife,

Sweden) and placed in EmbryoScope (Vitrolife, Sweden). Each embryo was imaged every 10

minutes, and its development events were annotated for up to 96 hours. Timing for embryo

developmental hallmarks were compared between the control and experimental groups. Resulting

blastocysts were transferred into a 2.5 dpc pseudo-pregnant CD-1 female mouse mated with

vasectomized CD-1 male mouse. Embryo transfer was conducted either surgically or by using a non-

surgical embryo transfer (NSET) device (ParaTechs, Lexington, KY, USA).[93] Delivered pups were

weighed and monitored until weaning.

Author contributions

A.M. was responsible for the conceptualization, data curation, methodology, investigation, validation

writing-original draft, device fabrication, review & editing; B.D. was responsible for device fabrication,

investigation, validation, device design and writing; P.X. was responsible for the animal studies and

writing; M.Y. was responsible for investigation, validation; Z.R. was responsible for supervision,

funding acquisition; A.L., G.P. and A.A. were responsible for project administration, funding

acquisition, writing-review & editing, and supervision.

Acknowledgments

References

655

656   1   L. F. Rienzi, R. Maggiulli and F. M. Ubaldi, in *In Vitro Fertilization: A Textbook of Current and*

657   *Emerging Methods and Devices*, eds. Z. P. Nagy, A. C. Varghese and A. Agarwal, Springer

658   International Publishing, Cham, 2019, pp. 133–145.

659   2   T. Ebner, in *In Vitro Fertilization: A Textbook of Current and Emerging Methods and Devices*,

660   eds. Z. P. Nagy, A. C. Varghese and A. Agarwal, Springer International Publishing, Cham, 2019,

661   pp. 471–479.

662   3   ESHRE Capri Workshop Group, *Hum. Reprod. Update*, 2007, **13**, 515–526.

663   4   A. R. Thornhill, C. E. deDie-Smulders, J. P. Geraedts, J. C. Harper, G. L. Harton, S. A. Lavery, C.

664   Moutou, M. D. Robinson, A. G. Schmutzler, P. N. Scriven, K. D. Sermon, L. Wilton and ESHRE

665   PGD Consortium, *Hum. Reprod.*, 2005, **20**, 35–48.

666   5   H. Schatten, Ed., *Germ Cell Protocols: Volume 2: Molecular Embryo Analysis, Live Imaging,*

667   *Transgenesis, and Cloning*, Humana Press, 2004.

668   6   K. Meyer, in *The Enzymes*, ed. P. D. Boyer, Academic Press, 1971, vol. 5, pp. 307–320.

669   7   Y. Ishizuka, T. Takeo, S. Nakao, H. Yoshimoto, Y. Hirose, Y. Sakai, Y. Horikoshi, S. Takeuji, S.

670   Tsuchiyama and N. Nakagata, *J. Reprod. Dev.*, 2014, **60**, 454–459.

671   8   B. R. L. de Moura, M. C. A. Gurgel, S. P. Machado, P. A. Marques, J. R. Rolim, M. C. de Lima

672   and L. L. Salgueiro, *JBRA Assist Reprod*, 2017, **21**, 27–30.

673   9   L. Rienzi, F. Ubaldi, F. Martinez, M. Iacobelli, M. G. Minasi, S. Ferrero, J. Tesarik and E. Greco,

674   *Hum. Reprod.*, 2003, **18**, 1289–1293.

675   10   S. Cooke, J. P. P. Tyler and G. L. Driscoll, *Hum. Reprod.*, 2003, **18**, 2397–2405.

676   11   C. Patrat, A. Kaffel, L. Delaroche, J. Guibert, P. Jouannet, S. Epelboin, D. De Ziegler, J.-P. Wolf

677   and P. Fauque, *Obstet. Gynecol. Int.*, 2012, **2012**, 403531.

678   12   D. Beebe, M. Wheeler, H. Zeringue, E. Walters and S. %J T. Raty, *Theriogenology*, 2002, **57**,

679   125–135.

680   13   M. Tokeshi, Ed., *Applications of Microfluidic Systems in Biology and Medicine*, Springer,

681   Singapore, 2019.

682 14 M. Yaghoobi, M. Azizi, A. Mokhtare and A. Abbaspourrad, *Lab Chip*, , DOI:10.1039/d1lc00091h.

683 15 H. C. Zeringue and D. J. Beebe, in *Germ Cell Protocols*, Springer, 2004, pp. 365–373.

684 16 H. C. Zeringue, J. J. Rutledge and D. J. Beebe, *Lab Chip*, 2005, **5**, 86–90.

685 17 L. Weng, G. Y. Lee, J. Liu, R. Kapur, T. L. Toth and M. Toner, *Lab Chip*, 2018, **18**, 3892–3902.

686 18 A. Mokhtare, P. Xie, A. Abbaspourrad, Z. Rosenwaks and G. Palermo, in *HUMAN*

687   *REPRODUCTION*, OXFORD UNIV PRESS GREAT CLARENDON ST, OXFORD OX2 6DP,

688   ENGLAND, 2020, vol. 35, pp. 71–72.

689 19 A. Mokhtare, P. Xie, A. Abbaspourrad, Z. Rosenwaks and G. D. Palermo, *Fertil. Steril.*, 2020,

690   **114**, e76.

691 20 J. E. Swain, D. Lai, S. Takayama and G. D. Smith, *Lab Chip*, 2013, **13**, 1213–1224.

692 21 A. Ozcelik, J. Rufo, F. Guo, Y. Gu, P. Li, J. Lata and T. J. Huang, *Nat. Methods*, 2018, **15**, 1021–

693   1028.

694 22 Z. Chen, X. Liu, M. Kojima, Q. Huang and T. Arai, *NATO Adv. Sci. Inst. Ser. E Appl. Sci.*, 2020,

695   **10**, 1260.

696 23 W. Connacher, N. Zhang, A. Huang, J. Mei, S. Zhang, T. Gopesh and J. Friend, *Lab Chip*, 2018,

697   **18**, 1952–1996.

698 24 J. P. Shelby and D. T. Chiu, *Lab Chip*, 2004, **4**, 168–170.

699 25 A. Fakhfouri, C. Devendran, T. Albrecht, D. J. Collins, A. Winkler, H. Schmidt and A. Neild, *Lab*

700   *Chip*, 2018, **18**, 2214–2224.

701 26 J. Friend and L. Y. Yeo, *Rev. Mod. Phys.*, 2011, **83**, 647–704.

702 27 G. Destgeer and H. J. Sung, *Lab Chip*, 2015, **15**, 2722–2738.

703 28 J. Hultström, O. Manneberg, K. Dopf, H. M. Hertz, H. Brismar and M. Wiklund, *Ultrasound Med.*

704   *Biol.*, 2007, **33**, 145–151.

705 29 F. S. Foster, C. J. Pavlin, K. A. Harasiewicz, D. A. Christopher and D. H. Turnbull, *Ultrasound*

706   *Med. Biol.*, 2000, **26**, 1–27.

707 30 M. A. Burguillos, C. Magnusson, M. Nordin, A. Lenshof, P. Augustsson, M. J. Hansson, E. Elmér,

708   H. Lilja, P. Brundin, T. Laurell and T. Deierborg, *PLoS One*, 2013, **8**, e64233.

709   31   V. Marx, *Nat. Methods*, 2015, **12**, 41–44.

710   32   M. Wiklund, *Lab Chip*, 2012, **12**, 2018–2028.

711   33   M. Mahadevan, K. Chalder, D. Wiseman, A. Leader and P. J. Taylor, *J. In Vitro Fert. Embryo*

712   *Transf.*, 1987, **4**, 277–280.

713   34   S. Lenz, J. G. Lauritsen and M. Kjellow, *Lancet*, 1981, **317**, 1163–1164.

714   35   A. Cardinale, R. Lagalla, V. Giambanco and F. Aragona, *Ultrasonics*, 1991, **29**, 261–263.

715   36   U. S. Food, D. Administration and Others, *Rockville, MD: FDA*.

716   37   D. L. Miller, N. B. Smith, M. R. Bailey, G. J. Czarnota, K. Hynynen, I. R. S. Makin and Bioeffects

717   Committee of the American Institute of Ultrasound in Medicine, *J. Ultrasound Med.*, 2012, **31**,

718   623–634.

719   38   Z. Xin, G. Lin, H. Lei, T. F. Lue and Y. Guo, *Transl. Androl. Urol.*, 2016, **5**, 255–266.

720   39   J. S. Abramowicz, in *Ultrasound Imaging in Reproductive Medicine: Advances in Infertility Work-*

721   *up, Treatment and ART*, eds. L. A. Stadtmauer and I. Tur-Kaspa, Springer International

722   Publishing, Cham, 2019, pp. 3–17.

723   40   M. A. Ghanem, A. D. Maxwell, Y.-N. Wang, B. W. Cunitz, V. A. Khokhlova, O. A. Sapozhnikov

724   and M. R. Bailey, *Proc. Natl. Acad. Sci. U. S. A.*, 2020, **117**, 16848–16855.

725   41   USPTO, 20200095529:A1, *US Patent*, 2020.

726   42   J. Park, B. H. Ha, G. Destgeer, J. H. Jung and H. J. Sung, *RSC Adv.*, 2016, **6**, 33937–33944.

727   43   M. Wiklund, R. Green and M. Ohlin, *Lab Chip*, 2012, **12**, 2438–2451.

728   44   M. B. Dentry, L. Y. Yeo and J. R. Friend, *Phys. Rev. E Stat. Nonlin. Soft Matter Phys.*, 2014, **89**,

729   013203.

730   45   P. Zhang, H. Bachman, A. Ozcelik and T. J. Huang, *Annu. Rev. Anal. Chem.* , 2020, **13**, 17–43.

731   46   M. Gedge and M. Hill, *Lab Chip*, 2012, **12**, 2998–3007.

732   47   A. R. Rezk, L. Y. Yeo and J. R. Friend, *Langmuir*, 2014, **30**, 11243–11247.

733   48   G. Destgeer, J. H. Jung, J. Park, H. Ahmed and H. J. Sung, *Anal. Chem.*, 2017, **89**, 736–744.

734   49   P. Zhang, C. Chen, X. Su, J. Mai, Y. Gu, Z. Tian, H. Zhu, Z. Zhong, H. Fu, S. Yang, K.

735   Chakrabarty and T. J. Huang, *Sci Adv*, 2020, **6**, eaba0606.

736   50 L. Schmid, A. Wixforth, D. A. Weitz and T. Franke, *Microfluid. Nanofluidics*, 2012, **12**, 229–235.

737   51 G. T. Silva, J. H. Lopes, J. P. Leão-Neto, M. K. Nichols and B. W. Drinkwater, *Phys. Rev.*

738   *Applied*, 2019, **11**, 054044.

739   52 B. W. Drinkwater, *Appl. Phys. Lett.*, 2020, **117**, 180501.

740   53 J. Bennès, S. Ballandras and F. Chérioux, *Appl. Surf. Sci.*, 2008, **255**, 1796–1800.

741   54 A. Winkler, R. Brünig, C. Faust, R. Weser and H. Schmidt, *Sens. Actuators A Phys.*, 2016, **247**,

742   259–268.

743   55 J. E. Michaels, S. J. Lee, A. J. Croxford and P. D. Wilcox, *Ultrasonics*, 2013, **53**, 265–270.

744   56 Y. J. Montagut, J. V. García, Y. Jiménez, C. March, A. Montoya and A. Arnau, *Rev. Sci. Instrum.*,

745   2011, **82**, 064702.

746   57 S. Assous, J. Rees, M. Lovell, L. Linnett and D. Gunn, *Advances in Piezoelectric Transducers*,

747   2011, 75.

748   58 R. T. Smith and F. S. Welsh, *J. Appl. Phys.*, 1971, **42**, 2219–2230.

749   59 R. J. Shilton, M. Travagliati, F. Beltram and M. Cecchini, *Adv. Mater.*, 2014, **26**, 4941–4946.

750   60 G. Destgeer, B. Ha, J. Park and H. J. Sung, *Anal. Chem.*, 2016, **88**, 3976–3981.

751   61 G. Destgeer, H. Cho, B. H. Ha, J. H. Jung, J. Park and H. J. Sung, *Lab Chip*, 2016, **16**, 660–667.

752   62 T. Hasegawa and K. Yosioka, *J. Acoust. Soc. Am.*, 1969, **46**, 1139–1143.

753   63 T. Hasegawa and K. Yosioka, *J. Acoust. Soc. Am.*, 1975, **58**, 581–585.

754   64 A. A. Doinikov, *Recent research developments in acoustics*, 2003, **1**, 39–67.

755   65 K. S. Wong, L. Lee, Y. M. Hung, L. Y. Yeo and M. K. Tan, *Anal. Chem.*, 2019, **91**, 12358–12368.

756   66 T. R. Nelson, J. B. Fowlkes, J. S. Abramowicz and C. C. Church, *J. Ultrasound Med.*, 2009, **28**,

757   139–150.

758   67 C. C. Church, C. Labuda and K. Nightingale, *Ultrasound Med. Biol.*, 2015, **41**, 472–485.

759   68 H. Ando, L. B. Feril Jr, T. Kondo, Y. Tabuchi, R. Ogawa, Q.-L. Zhao, Z.-G. Cui, S.-I. Umemura, H.

760   Yoshikawa and T. Misaki, *Cancer Lett.*, 2006, **242**, 37–45.

761   69 Y. Feng, Z. Tian and M. Wan, *J. Ultrasound Med.*, 2010, **29**, 963–974.

762   70   K. H. Ng, *J. Med. Ultrasound*, 2002, **10**, 5–9.

763   71   E. Lucena and H. Moreno-Ortiz, in *Development of In Vitro Maturation for Human Oocytes:*

764   *Natural and Mild Approaches to Clinical Infertility Treatment*, eds. R.-C. Chian, G. Nargund and J.

765   Y. J. Huang, Springer International Publishing, Cham, 2017, pp. 267–279.

766   72   P. S. Balasubramanian, A. Singh, C. Xu and A. Lal, *Sci. Rep.*, 2020, **10**, 3075.

767   73   L. E. Houston, A. O. Odibo and G. A. Macones, *Prenat. Diagn.*, 2009, **29**, 1204–1212.

768   74   M. W. Miller, W. L. Nyborg, W. C. Dewey, M. J. Edwards, J. S. Abramowicz and A. A. Brayman,

769   *Int. J. Hyperthermia*, 2002, **18**, 361–384.

770   75   Z. Izadifar, P. Babyn and D. Chapman, *Ultrasound Med. Biol.*, 2017, **43**, 1085–1104.

771   76   R. J. Shilton, V. Mattoli, M. Travagliati, M. Agostini, A. Desii, F. Beltram and M. Cecchini, *Adv.*

772   *Funct. Mater.*, 2015, **25**, 5895–5901.

773   77   T. Zheng, C. Wang, Q. Hu and S. Wei, *Appl. Phys. Lett.*, 2018, **112**, 233702.

774   78   M. Baudoin, J.-L. Thomas, R. A. Sahely, J.-C. Gerbedoen, Z. Gong, A. Sivery, O. B. Matar, N.

775   Smagin, P. Favreau and A. Vlandas, *Nat. Commun.*, 2020, **11**, 4244.

776   79   S. Collignon, O. Manor and J. Friend, *Adv. Funct. Mater.*, 2018, **28**, 1704359.

777   80   J. Kubanek, J. Shi, J. Marsh, D. Chen, C. Deng and J. Cui, *Sci. Rep.*, 2016, **6**, 24170.

778   81   A. Lervik, S. Kjelstrup and H. Qian, *Phys. Chem. Chem. Phys.*, 2015, **17**, 1317–1324.

779   82   K. Länge, B. E. Rapp and M. Rapp, *Anal. Bioanal. Chem.*, 2008, **391**, 1509–1519.

780   83   X. H. (孔祥华) Kong, C. Deneke, H. Schmidt, D. J. Thurmer, H. X. (季恒星) Ji, M. Bauer and O. G.

781   Schmidt, *Appl. Phys. Lett.*, 2010, **96**, 134105.

782   84   S. H. Weinberg, *PLoS One*, 2013, **8**, e81402.

783   85   A. R. Rezk, H. Ahmed, T. L. Brain, J. O. Castro, M. K. Tan, J. Langley, N. Cox, J. Mondal, W. Li,

784   M. Ashokkumar and L. Y. Yeo, *J. Phys. Chem. Lett.*, 2020, **11**, 4655–4661.

785   86   G. Peyré, *IEEE Computing in Science and Engineering*, 2011, **13**, 94–97.

786   87   R. S. Sengar, A. K. Upadhyay, M. Singh and V. M. Gadre, *Biomed. Signal Process. Control*,

787   2016, **25**, 62–75.

788 88 R. S. Sengar, A. K. Upadhyay, M. Singh and V. M. Gadre, in *2012 National Conference on*

789   *Communications (NCC)*, ieeexplore.ieee.org, 2012, pp. 1–5.

790 89 A. K. Upadhyay, Ashutosh Kumar Upadhyay (2021). Wavelet Based Image Segmentation,

791   https://www.mathworks.com/matlabcentral/fileexchange/48610-wavelet-based-image-

792   segmentation, (accessed March 8, 2021).

793 90 J. Costa, S. McHugh, N. Rice, P. J. Turner, B. A. Willemsen, N. O. Fenzi, R. B. Hammond, J. D.

794   Ha, C. H. Lee and T. Sato, in *2017 IEEE International Ultrasonics Symposium (IUS)*, 2017, pp. 1–

795   4.

796 91 Home - Embryotech Laboratories Inc, https://embryotech.com/, (accessed March 4, 2021).

797 92 N. Yoshida and A. C. F. Perry, *Nat. Protoc.*, 2007, **2**, 296–304.

798 93 M. Green, S. Bass and B. Spear, *Biotechniques*, 2009, **47**, 919–924.